

Acoustic wave propagation in the solar sub-photosphere with localised magnetic field concentration: effect of magnetic tension

S. Shelyag, S. Zharkov, V. Fedun, R. Erdélyi, M.J. Thompson

Solar Physics and Space Plasma Research Center, Department of Applied Mathematics, University of Sheffield, Hicks Building, Hounsfield Rd., Sheffield, S7 3RH, United Kingdom

01.01.01/01.01.01

ABSTRACT

Aims. In this paper we analyse numerically the propagation and dispersion of acoustic waves in the solar-like sub-photosphere with localised non-uniform magnetic field concentrations, mimicking sunspots with various representative magnetic field configurations.

Methods. Numerical simulations of wave propagation through the solar sub-photosphere with a localised magnetic field concentration are carried out using SAC, which solves the MHD equations for gravitationally stratified plasma. The initial equilibrium density and pressure stratifications are derived from a standard solar model. Acoustic waves are generated by a source located at the height approximately corresponding to the visible surface of the Sun. We analyse the response of vertical velocity to changes in the interior due to magnetic field at the level corresponding to the visible solar surface, by the means of local time-distance helioseismology.

Results. The results of numerical simulations of acoustic wave propagation and dispersion in the solar sub-photosphere with localised magnetic field concentrations of various types are presented. Time-distance diagrams of the vertical velocity perturbation at the level corresponding to the visible solar surface show that the magnetic field perturbs and scatters acoustic waves and absorbs the acoustic power of the wave packet. For the weakly magnetised case the effect of magnetic field is mainly thermodynamic, since the magnetic field changes the temperature stratification. However, we observe the signature of slow magnetoacoustic mode, propagating downwards, for the strong magnetic field cases.

Key words. Sun: helioseismology — Sun: magnetic fields — Sun: oscillations — Sun: photosphere — (Sun:) sunspots

1. Introduction

The internal structure of sunspots is still not well known. Helioseismological techniques, which analyse the influence of internal solar inhomogeneities on sound wave propagation and the signatures of such waves at the solar surface, might be of great help in revealing the invisible, sub-photospheric solar processes. The ability of forward numerical simulations to predict and model a number of solar phenomena in helioseismology has been shown by e.g. Shelyag et al. (2006, 2007); Hanasoge et al. (2007); Parchevsky & Kosovichev (2007) and others. As magnetic fields are, perhaps, the most important property of many solar features, a new and rapidly developing field is the study of the influence of magnetic fields on acoustic wave propagation of solar magnetic field concentrations such as sunspots or solar active regions. The appearance and importance of slow magnetoacoustic waves has been shown in forward MHD simulations in polytropic models by Crouch & Cally (2003); Gordovskyy & Jain (2007); Moradi et al. (2009). Ray-approximation simulations in a more realistic and applicable magnetised model have shown a similar behaviour to the acoustic waves (Moradi & Cally, 2008). Shelyag et al. (2007) have investigated the influence of sub-photospheric flows on acoustic wave propagation using forward modelling and demonstrated a discrepancy between the actual flow profiles and the flow profiles obtained by ray-approximation inversion. The simulations of a wave packet, constructed from f -modes, which was carried out

by Cameron et al. (2008), have shown a good agreement with helioseismological observations of sunspots. Now it is timely to perform a full forward magneto-hydrodynamic simulation of a wave packet propagating through a non-uniform magnetic field region in the solar sub-photosphere with a realistic temperature profile.

In the simulations presented here we consider three different representative configurations of solar magnetic field. Each of the cases has a common feature that the field is spatially localised, allowing a direct comparison of the travel speeds and time differences of the wave propagation between the magnetised and non-magnetised solar plasma. The representative configurations differ in both magnetic field strength and geometry. Their spatial structure affects the temperature stratification of the simulated sunspot by the magnetic tension. We selected two representative strong field configurations with opposite effects on the temperature in the sunspot: one, where the magnetic-field curvature is strong and, thus, increases the temperature in the magnetic field region; and another, where the magnetic field curvature is small, and the temperature is decreased in the sunspot. The magnetic configurations we apply are in magnetohydrostatic equilibrium with the ambient external plasma. These two-dimensional magnetic fields are self-similar and non-potential.

We present the results according to the following general structure. Section 2 briefly describes the numerical techniques that we have used to carry out the simulations. The configurations of the magnetic fields and initial configura-

tion for the simulations are described in Section 3. The source used to generate the acoustic modes in the numerical domain is presented in Section 4. Section 5 is devoted to (i) the techniques of helioseismological analysis we have used, and (ii) the results we obtained. Section 6 concludes.

2. Simulation model

The code SAC (Sheffield Advanced Code) has been developed by Shelyag et al. (2008) to carry out numerical studies. The code is based on VAC (Versatile Advection Code, Tóth et al., 1998), however, it employs artificial diffusivity and resistivity in order to stabilise the numerical solutions. Also, SAC uses the technique of variable separation to background and perturbed components to treat gravitationally stratified plasma. According to Shelyag et al. (2008), if a plasma is assumed to be in magnetohydrostatic equilibrium given by

$$(\mathbf{B}_b \cdot \nabla) \mathbf{B}_b + \nabla \frac{\mathbf{B}_b^2}{2} + \nabla p_b = \rho_b \mathbf{g}, \quad (1)$$

the system of MHD equations governing arbitrary perturbations of density, momentum, energy and magnetic field is written as follows:

$$\frac{\partial \tilde{\rho}}{\partial t} + \nabla \cdot [\mathbf{v}(\rho_b + \tilde{\rho})] = 0 + D_\rho(\tilde{\rho}), \quad (2)$$

$$\frac{\partial[(\rho_b + \tilde{\rho})\mathbf{v}]}{\partial t} + \nabla \cdot [\mathbf{v}(\rho_b + \tilde{\rho})\mathbf{v} - \tilde{\mathbf{B}}\tilde{\mathbf{B}}] - \nabla \cdot [\tilde{\mathbf{B}}\mathbf{B}_b + \mathbf{B}_b\tilde{\mathbf{B}}] + \nabla \tilde{p}_t = \tilde{\rho}\mathbf{g} + \mathbf{D}_{\rho v}[(\tilde{\rho} + \rho_b)\mathbf{v}], \quad (3)$$

$$\frac{\partial \tilde{e}}{\partial t} + \nabla \cdot [\mathbf{v}(e + e_b) - \tilde{\mathbf{B}}\tilde{\mathbf{B}} \cdot \mathbf{v} + \mathbf{v}\tilde{p}_t] - \nabla \cdot \left[(\tilde{\mathbf{B}}\mathbf{B}_b + \mathbf{B}_b\tilde{\mathbf{B}}) \cdot \mathbf{v} \right] + p_{tb}\nabla \cdot \mathbf{v} - \mathbf{B}_b\mathbf{B}_b \nabla \cdot \mathbf{v} = \tilde{\rho}\mathbf{g} \cdot \mathbf{v} + D_e(\tilde{e}), \quad (4)$$

$$\frac{\partial \tilde{\mathbf{B}}}{\partial t} + \nabla \cdot [\mathbf{v}(\tilde{\mathbf{B}} + \mathbf{B}_b) - (\tilde{\mathbf{B}} + \mathbf{B}_b)\mathbf{v}] = 0 + \mathbf{D}_B(\tilde{\mathbf{B}}), \quad (5)$$

where $\tilde{\rho}$ and ρ_b are the perturbation and background density counterparts, \mathbf{v} is the total velocity vector, e is the total background energy density per unit volume, \tilde{e} is the perturbed energy density per unit volume, \mathbf{B}_b and $\tilde{\mathbf{B}}$ are the background and perturbed magnetic field vectors, p_{tb} is the total (magnetic + kinetic) background pressure, γ is the adiabatic gas index, \mathbf{g} is the external gravitational field vector, and \tilde{p}_t is the perturbation to the total pressure

$$\tilde{p}_t = \tilde{p}_k + \frac{\tilde{\mathbf{B}}^2}{2} + \mathbf{B}_b\tilde{\mathbf{B}}, \quad (6)$$

or, in terms of perturbed energy density per unit volume \tilde{e} ,

$$\tilde{p}_k = (\gamma - 1) \left(\tilde{e} - \frac{(\rho_b + \tilde{\rho})\mathbf{v}}{2} - \mathbf{B}_b\tilde{\mathbf{B}} - \frac{\tilde{\mathbf{B}}^2}{2} \right), \quad (7)$$

and

$$\tilde{p}_t = (\gamma - 1) \left[\tilde{e} - \frac{(\rho_b + \tilde{\rho})\mathbf{v}}{2} \right] - (\gamma - 2) \left(\mathbf{B}_b\tilde{\mathbf{B}} + \frac{\tilde{\mathbf{B}}^2}{2} \right). \quad (8)$$

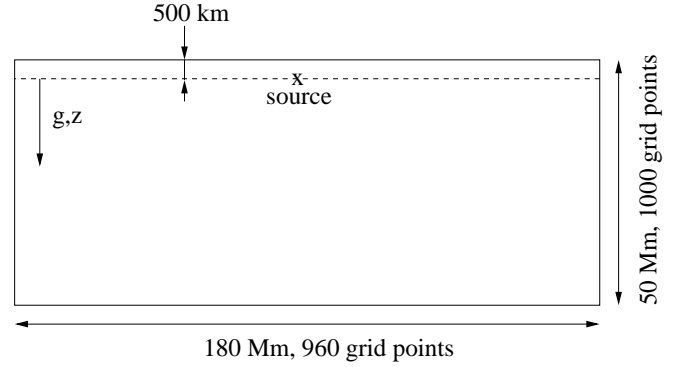


Fig. 1. Sketch of the simulation domain geometry, used in the simulations.

Here p_{tb} denotes the total background pressure

$$p_{tb} = p_{kb} + \frac{\mathbf{B}_b^2}{2} \quad (9)$$

which, in terms of background conservative variables, gives

$$p_{kb} = (\gamma - 1) \left(e_b - \frac{\mathbf{B}_b^2}{2} \right), \quad (10)$$

and

$$p_{tb} = (\gamma - 1) e_b - (\gamma - 2) \frac{\mathbf{B}_b^2}{2}. \quad (11)$$

Eqs. (2)-(11) are solved using a fourth-order central difference scheme for the spatial derivatives and are advanced in time by implementing a fourth order Runge-Kutta numerical method. The source terms D in the right-hand sides of the equations denote the artificial diffusivity and resistivity terms. The simulation domain is shown in Fig. 1. The 2D box is 180 Mm wide and 50 Mm deep, and has a resolution of 960x1000 grid points; the upper boundary of the domain is at the solar surface $R = R_\odot$. The boundaries of the domain are open. The perturbation source is located in the upper-middle (500 km below the upper boundary) of the simulation box. The synthetic measurement level is located at the solar surface.

3. Magnetic fields and initial conditions

For an initial background model, we adopt the Standard Model S (Christensen-Dalsgaard et al., 1996). The model is then adjusted to have the same temperature stratification as the Standard Model, if the constant adiabatic constant Γ_1 is taken. According to the Standard Model S, the pressure at the solar surface $R = R_\odot$ is equal to $p_\odot = 7.61 \cdot 10^4$ dyn/cm². This creates an upper limit for the vertical straight uniform magnetic field in the magnetohydrostatic equilibrium with non-magnetic external plasma to be about $B_{max} = \sqrt{8\pi p_\odot} = 1.4$ kG. The measured magnetic field strength in sunspot umbrae is about 2.5–3.5 kG, which suggests the implementation of curved magnetic fields in the simulations. In the case of curved magnetic field, magnetic tension balances magnetic pressure, thus increasing the upper limit for the equilibrium magnetic field. An example of such balance is a potential magnetic field, where the magnetic tension is exactly equal to the magnetic pressure: such a field does not change background pressure and

density equilibrium. However, the potential magnetic fields have a disadvantage for numerical modelling. If a potential magnetic field is considered, the boundaries of the numerical domain should be either fixed or periodic to confine the magnetic field and prevent it from strong expansion.

We use a self-similar non-potential magnetic field configuration (Schlüter & Temesváry, 1958; Schüssler & Rempel, 2005; Cameron et al., 2008), which can be obtained from the following set of equations:

$$B_x = -\frac{\partial f}{\partial z} \cdot G(f), \quad (12)$$

$$B_z = \frac{\partial f}{\partial x} \cdot G(f), \quad (13)$$

and

$$f = x \cdot B_{0z}(z), \quad (14)$$

where B_{0z} describes the decrease of the vertical component of magnetic field towards the top of the model, and G is the function which defines how the magnetic field opens up with height. The magnetic field constructed in this way is divergence-free by definition. The equilibrium background gas pressure and density are then recalculated using the magnetohydrostatic equilibrium condition Eq. (1). If the magnetic field \mathbf{B}_b is prescribed, Eq. (1) splits into two independent equations for the pressure and density deviations from the initial state, caused by the magnetic field. These equations are then solved numerically in order to obtain the gravitationally stratified plasma model with localised magnetic field concentration in magnetohydrostatic equilibrium.

Three characteristic situations, mimicking sunspots which differ by the magnetic field strength at the visible solar surface and curvature of the magnetic field, are chosen for helioseismic analysis: weak but strongly-curved magnetic field ($B_{z,\odot} = 120$ G, Case A), strong but weakly-curved magnetic field with $B_{z,\odot} = 3.5$ kG (Case B), and strongly-curved strong magnetic field ($B_{z,\odot} = 3.5$ kG, Case C). The magnetic field structures for these situations are shown in Figs. 2-4.

The curvature of magnetic field changes the temperature stratification in the domain. For the first case of the weak magnetic field (Case A, Fig. 2), the temperature change is rather small (Fig. 5). Below the temperature decrease, which is caused by the drop of the kinetic pressure in the region where the magnetic field is nearly vertical, a temperature increase is noticeable. This increase is caused by the pressure rise which is needed to compensate the increase in magnetic tension.

The two initial configurations with strong magnetic field show these processes in greater detail. For Case B (weakly-curved magnetic field, Fig. 2), the temperature is considerably decreased beneath the solar surface (Fig. 6), because the magnetic field is nearly vertical at the surface. The effect of magnetic tension reveals itself in the strongly-curved magnetic field configuration (Case C, Fig. 7). Here, in this latter case, the temperature deviation $\Delta T/T$ is mainly positive.

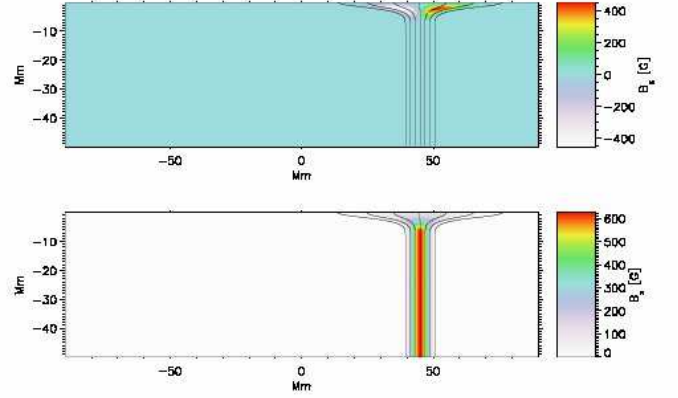


Fig. 2. Magnetic field configuration for the case of weak magnetic field (Case A) in the sub-photospheric domain of the size of 50 Mm in vertical and 180 Mm in horizontal direction. The horizontal (B_x) and vertical (B_z) components of the magnetic field are shown. The field lines are overplotted.

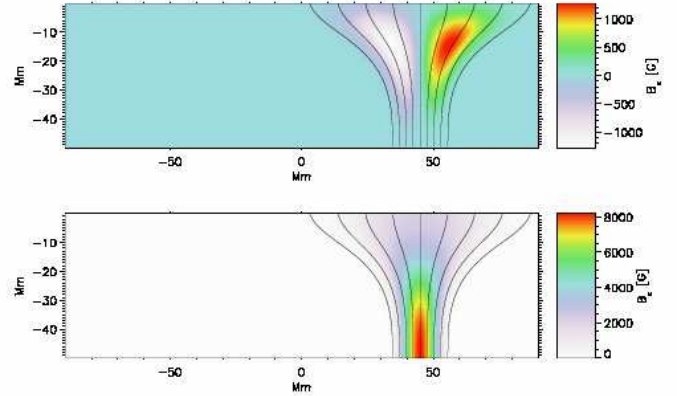


Fig. 3. Same as Fig. 2, with a strong magnetic flux ($B_{z,\odot} = 3.5$ kG) but with weakly-curved magnetic field lines, Case B.

4. Acoustic source

To generate acoustic waves, we introduce a perturbation source described by the expression:

$$v_z = A_0 \sin \frac{2\pi t}{T_0} \exp \left(-\frac{(t - T_1)^2}{\sigma_1^2} \right) \exp \left(-\frac{(r - r_0)^2}{\sigma_0^2} \right), \quad (15)$$

where $T_0=300$ s, $T_1=600$ s, $\sigma_1=100$ s, $\sigma_2=0.1$ Mm, r_0 is the source location. The source is located in the middle of the horizontal layer slightly beneath the solar surface (see Fig. 1). The amplitude of the source A_0 is chosen to be sufficiently small, which ensures that convective processes will not be initiated in the otherwise convectively unstable equilibrium, and that the perturbation is still linear, i.e. does not change the background strongly. The source generates a temporally localised wave packet with the duration of about 600 s, which has the main frequency of about 3.33 mHz.

The acoustic response of the simulation box to the source is shown in Fig. 8. It is evident from the figure that the source generates a whole branch of various solar acoustic modes. The p -modes are visible up to high orders.

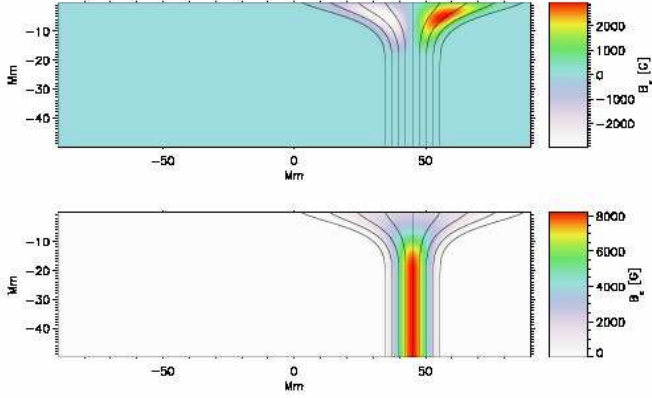


Fig. 4. Same as Fig. 2, with a strongly-curved, strong ($B_{z,\odot} = 3.5$ kG) magnetic field, Case C.

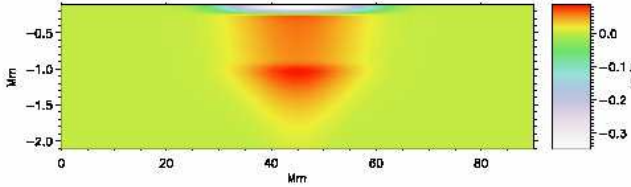


Fig. 5. Zoom-in of the temperature difference in the magnetic field region for Case A. The temperature increase is caused by magnetic tension.

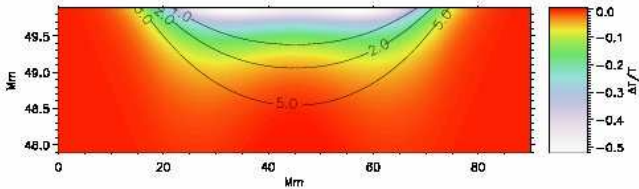


Fig. 6. Same as Fig. 5, with a strong magnetic flux and weakly-curved magnetic field lines, Case B. Here, the temperature decreases at the solar surface. This temperature decrease is caused by magnetic pressure. Plasma β contours with levels $\beta = 1, 2, 5$ are overlotted.

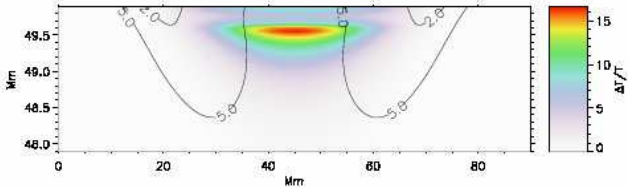


Fig. 7. Same as Fig. 5, with the strongly-curved and strong magnetic field, Case C. In this case magnetic tension prevents evacuation of the magnetic region, and the temperature is increased.

Also, in order to check the validity of the simulations, the one-dimensional calculation of the eigenmodes of the initial background model was performed. The corresponding eigenfrequencies are overlotted in the figure (solid lines). A small difference between the model and the observed frequencies is caused by discrepancies between the Standard Model S and the model implemented here, which

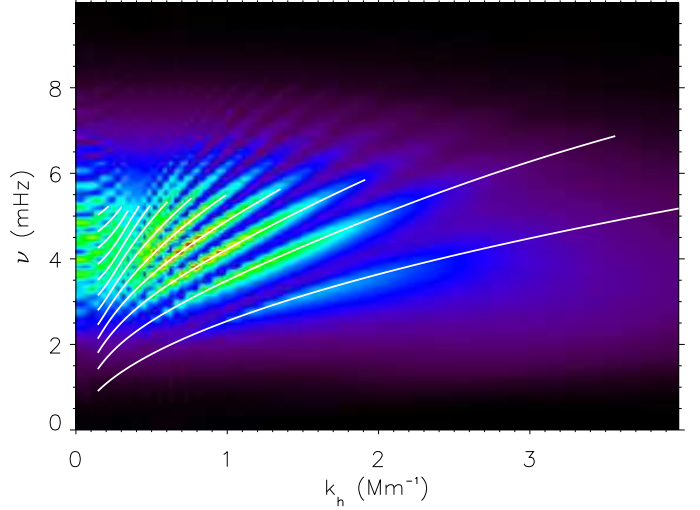


Fig. 8. Power spectrum of the vertical velocity perturbation generated by the source. The p modes are visible up to high orders. Eigenmodes of the background model are overlotted by solid lines.

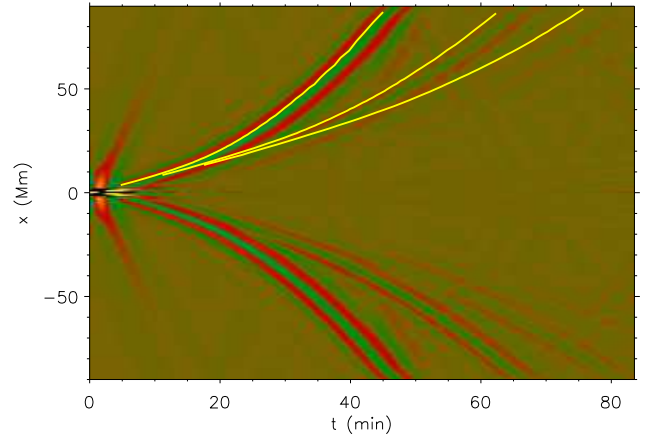


Fig. 9. Cross-correlation function deduced from the vertical velocity perturbation at the solar surface, generated by the acoustic source. Three wave bounces are clearly visible. Group travel times for the first three bounces deduced from ray theory are overlotted.

is accountable for using the equation of state for an ideal gas. However, we leave the development of non-ideal equation of state, including the ionisation processes, and correction of these discrepancies for a future work, since they will not play any major role in the calculations of the influence of non-uniform magnetic fields on acoustic wave propagation in the solar photosphere.

Next, Fig. 9 shows the time-distance diagram computed at the simulated solar surface via cross-correlating the vertical velocity component, generated by the acoustic source. Three wave bounces are clearly visible on the plot. Some weak and artificial reflection from the side boundaries, which is caused by not perfectly transparent boundaries of the numerical domain, is also noticeable.

5. Time-distance analysis

It has been mentioned above that the acoustic source is located in the middle of the horizontal layer close to the solar surface. This allows us to study the influence of the magnetic field on the acoustic response of the simulated solar sub-photosphere by comparing the plasma velocities to the left (non-magnetic part of the domain) and to the right (where the magnetic field is implemented) from the source. Similar technique has already been proposed and used by Shelyag et al. (2007) to reveal the discrepancies between the real and inverted velocity profiles for the sub-photosphere with embedded sub-photospheric horizontal flows.

The vertical velocity differences are computed between the points, located at the same distance to the left and to the right from the source. The difference images, obtained in this way, reveal the phase shifts and amplitude changes the wave packets experience due to the propagation in the magnetised region, compared to the non-magnetised one.

In each case of a magnetic configuration we compute the acoustic power of the vertical component of the velocity oscillations over the period of the simulation as function of horizontal and depth coordinates,

$$a_p(x, z) = \int v_z^2(x, z, t) dt,$$

and then consider the ratio between the corresponding points of the quiet Sun and perturbed parts of the model. A cut at the surface level corresponds to the acoustic power measurements deduced observationally. In addition, we have measured the travel time perturbations by cross-correlating the velocity signal at the source location with the signal at the target location, taking the quiet Sun cross-correlation function as a reference and using both Gábor wavelet fitting (Kosovichev & Duvall, 1997) or linearised definition outlined by Gizon & Birch (2002).

In the sections 5.1-5.3 we analyse by these means the wave propagation through the three cases of magnetic field structures. In the section 5.4, the results are compared.

5.1. Weak magnetic field (Case A)

The analysis shows that for the configuration of a weak magnetic field (Fig. 2) the influence the magnetic field exercises on the wave propagation is mainly caused by temperature (and hence local sound speed) changes in the magnetised region. The temperature increase below the simulated sunspot (see Fig. 5) causes negative phase shifts of the wave packets propagating through the magnetic structure.

In Fig. 10 small phase shifts are observed in all of the bounces, however, the first bounce wave is only affected in the magnetic field region (the phase shifts for the first bounce at 0-30 Mm and at 70-90 Mm are of the order of numerical noise). It was found that higher order bounces are all affected from 30 Mm distance onwards from the source.

In Fig. 11 we present the acoustic power ratio measured in the vertical velocity as a function of two spatial coordinates between the waves propagating in the quiet Sun and in the perturbed part of the model. We found that the power deficit at the location of the flux tube is confined to the uppermost layers of the model with the acoustic power ratio falling the closer to the surface one measures at. The ratio is constant and equal to unity to the left of the flux

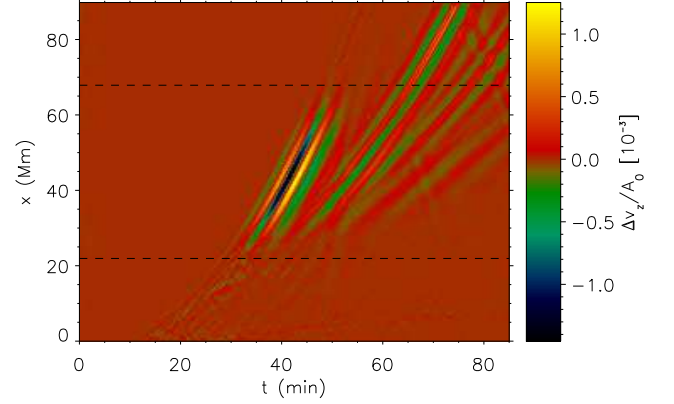


Fig. 10. Vertical speed difference image for Case A. Difference values are computed between points located at the same distance but opposite sides of the source. Two dashed lines bound the magnetic region with $|B| > 25$ G. The first bounce (leftmost in the figure) is affected only locally by the magnetic field, however, the second and third bounces are also affected in the 60-80 Mm distance region.

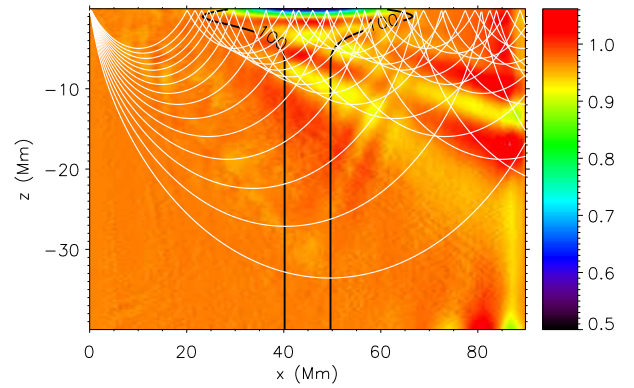


Fig. 11. Synthetic acoustic power ratio image for the weakly magnetised region of the weakly magnetised model (Case A). The ratios are computed between the points located at the same distance and opposite sides from the source. The image shows the regions of acoustic power decreased compared with the ambient non-magnetic medium. The black lines are the contours of vertical magnetic field at 50 and 100 G, respectively. The acoustic rays for e.g. the frequency $f = 4.5$ mHz computed for the quiet Sun model are also overplotted.

tube, while to the right we observe variations in the acoustic power at depths of 3 Mm and lower, extending along the straight lines starting below the surface at the flux tube boundary. From the overplotted acoustic rays computed for the unperturbed model we find that these lines agree well with the second and third bounce ray envelopes.

5.2. Weakly-curved, strong magnetic field (Case B)

In Case B (see Fig. 3), the temperature distribution is such that the temperature decreases in the sunspot region (Fig. 6), similarly to Case A, since the magnetic tension is relatively small. Again, as for Case A, accordingly to the

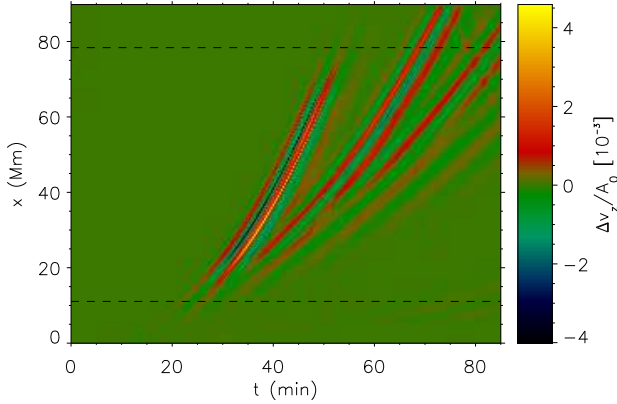


Fig. 12. Same as Fig. 10 but for the strong weakly-curved magnetic field ($B_{z,\odot} = 3.5$ kG), case B. Two dashed lines bound the magnetic region with $|B| > 250$ G.

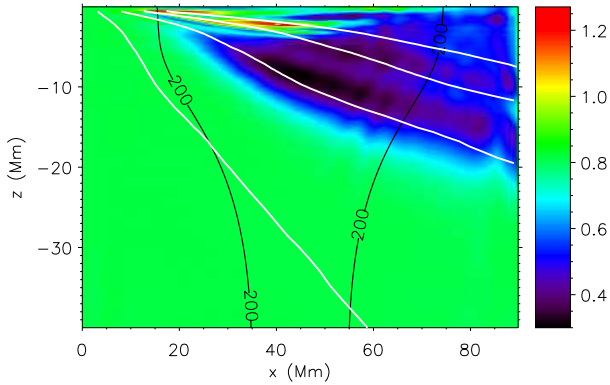


Fig. 13. Kinetic energy density ratio for the strong magnetic flux but weakly-curved magnetic field lines, Case B. The lower turning points for the first four bounces of rays emanating from the source are overplotted in white color. The black lines are the contours of the magnetic field $|B| = 200$ G.

vertical velocity difference image Fig. 12, the first bounce is affected by the magnetic field only in the magnetic field region. It is found that the second and higher-order bounces carry information about the interaction with magnetic field also in the non-magnetic or weakly magnetised sub-surface regions. Intuitively, following the temperature structure, a delay in arrival time of the wave packet at a distance from the source is expected, since the sound speed in the simulated sunspot is lower than in the non-magnetic surrounding plasma. A more detailed analysis nicely confirms this expectation. The first ridge in the image of velocity difference is positive, meaning that the wave arrives later at the point in the sunspot when compared with the counterpart wave that arrives at the same distance in the non-magnetic plasma.

In Case B, the slow magneto-acoustic mode is also observed in the domain (see Fig. 14). Generally, the slow-wave motions follow the magnetic field structure and shape. Further, a suppression of oscillations is observed at the surface in the magnetised region. At the distance of 40 Mm to the right from the source, the amplitude ratio of horizontal

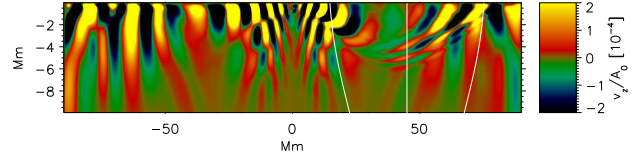


Fig. 14. Snapshot of the horizontal component of the velocity field in the upper layers of the domain, taken at $t = 5130$ s of the simulation for Case B. The slow mode is visible in the magnetised region beneath the solar surface between $x = 20$ Mm and $x = 70$ Mm. The magnetic field lines are overplotted.

velocity oscillations at the surface to the source amplitude A_0 is about 0.0001, while at the distance of -40 Mm to the left from the source it is more than 0.0004 (note that the image is overexposed in order to reveal the small amplitude structures). Thus, a significant part of oscillation energy transforms into slow magnetoacoustic wave motion, which propagates downwards along the magnetic field lines, and is taken out from the surface.

The kinetic energy density ratio plot (Fig. 13) shows the lines of decreased ratio, similar to Case A, with the structure immediately below the surface of the tube showing greater complexity than before, perhaps, due to the effect of magnetoacoustic waves. Fig. 13 also shows the curves corresponding to lower turning points for the first four bounces of the quiet Sun rays. Note that only the second, third and fourth bounce turning points correspond to the ray envelopes (see Fig. 11), representing caustic surfaces (Kravtsov & Orlov, 1993).

5.3. Strongly-curved, strong magnetic field (Case C)

Strong magnetic tension in Case C (Fig. 4) changes the kinetic gas pressure in a way that the temperature (and hence sound speed) in the sunspot region increases (see Fig. 7). As expected, the sound speed increase leads to a faster wave propagation through the magnetised region. Correspondingly, the vertical speed difference image (Fig. 15) shows a negative sign of the first ridge in the first bounce. Similar to the previous cases, the first bounce is affected by magnetic field only in the magnetic region (20 – 70 Mm distance), and the second and higher order bounces are affected everywhere after 20 Mm onwards.

For this case we measured the oscillatory power in pressure perturbation, scaled by inverse square root of the initial local density ρ_b , which is presented in Fig. 16. The same straight line structure, as in Cases A and B, is observed.

As in the previous case (Fig. 14), despite the plasma $\beta = 1$ surface does not appear in the domain, the slow magnetoacoustic mode of roughly the same amplitude, as for the weakly-curved magnetic field, is observed in the horizontal velocity component (Fig. 17). This surprising fact suggests that the conversion of acoustic waves into slow magneto-acoustic ones is nearly as efficient as in the case, where the plasma $\beta = 1$ surface is located in the domain. However, here the amplitude of horizontal velocity component in the magnetic region is larger, than in the case of weakly-curved strong magnetic field.

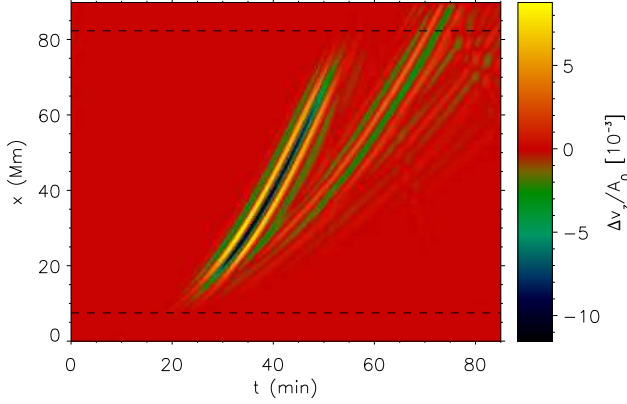


Fig. 15. Same as Fig. 10, but for the strongly-curved, strong magnetic field (Case C). Two dashed lines bound the magnetic region with $|B| > 250\text{G}$.

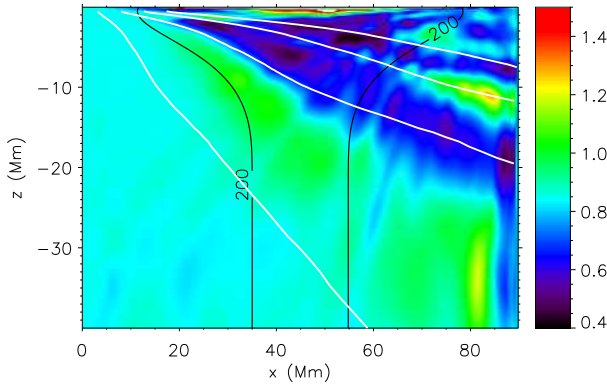


Fig. 16. Oscillatory power in pressure perturbation, scaled by inverse square root of the initial local density ρ_b , for the strongly-curved, strong magnetic field (Case C).

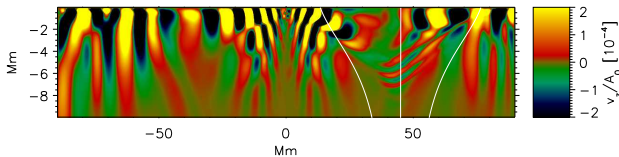


Fig. 17. Same as Fig. 14, for the strongly-curved strong magnetic field, case C. The slow mode is visible between the overplotted magnetic field lines.

5.4. Overall comparison of the effect of magnetic field structures on wave propagation

In the previous sections we have shown that a magnetic field of the same strength acts differently on acoustic waves depending on the geometry and curvature of the field. Here we summarise the findings by showing the travel time difference and wave packet amplitude dependencies for the representative three analysed cases.

We have measured the travel time perturbations for the generated waves when travelling through the flux tube using both Gábor wavelet and the Gizon-Birch definitions. A similar technique was applied by Thompson & Zharkov

(2008). The so-called Gizon-Birch travel time difference plots are shown in Fig. 18 for all three magnetic field cases, respectively. Each plot shows that the sign of travel time difference, calculated for the first bounce, changes correspondingly to the sign of the temperature difference caused by the magnetic field curvature. The travel time differences, obtained for the simulation with the weakly-curved strong magnetic field (Case B), are of the same order of those obtained from the observations (Duvall et al., 1997; Hughes et al., 2005; Zharkov et al., 2007). This fact suggests that the magnetic configuration, used for this simulation, is close to the magnetic field structures in the real sunspots.

Fig. 19 demonstrates the difference in the acoustic power absorption and suppression by the three different magnetic field configurations at the solar surface. The green curve corresponds to Case A. The oscillatory power suppression in the magnetic field region reaches 30%, however, no energy absorption is observed, since the power ratio at the distance $x = 80\text{ Mm}$ is close to unity. This fact, together with the absence of noticeable slow magnetoacoustic mode in the horizontal component of velocity, confirms our suggestion that the weak magnetic fields act only as temperature and sound speed perturbations for the waves propagating through the fields.

The power ratio for Case C (Fig. 19, red curve) is rather different. A very strong suppression of plasma motions in the magnetic field region (up to 90%) is observed. This suppression is caused by the strongly increased temperature in the simulated sunspot. Also, the energy absorption of about 5% is obtained at $x = 80\text{ Mm}$. This confirms the partial conversion of the wave packet energy into slow magnetoacoustic mode, which propagates downwards and removes the energy from the solar surface.

An even more complicated behavior is demonstrated by the acoustic power ratio at the solar surface, calculated for Case B (Fig. 19, black curve). In this case, the absorption reaches the value of about 10% at $x = 80\text{ Mm}$. The character of energy suppression in the magnetic field region is also different. The first feature here is that the curve is not symmetric with respect to the vertical axis of the magnetic field configuration (note that the green curve, corresponding to the weak magnetic field (Case A) is completely symmetric around the axis, and the red curve is also nearly symmetric, if the energy absorption is not taken into account). We suggest that the wavy structure between $x = 35\text{ Mm}$ and $x = 50\text{ Mm}$ is connected to the conversion of purely acoustic wave into slow magnetoacoustic mode. However, the most noticeable feature of this curve is the acoustic power increase of the order of 7-8% at the distance $x = 60\text{ Mm}$. This feature is also clearly visible in the two-dimensional power image (Fig. 13), and can be compared with acoustic power haloes around sunspots, usually observed (see, for example, recent observations by Hill et al. (2001) or Nagashima et al. (2007) using new instrument Hinode, and references therein).

The straight lines emanating at different angles from the flux tubes' left boundary to the right edge of the box, visible in both oscillatory power plots for vertical velocity component, kinetic energy and pressure perturbation, in our view can be explained in terms of the ray theory as the caustic surface changes occurring due to the sound-speed inhomogeneity in the x -direction. There are caustics corresponding to the envelope to the ray paths for the second and higher-

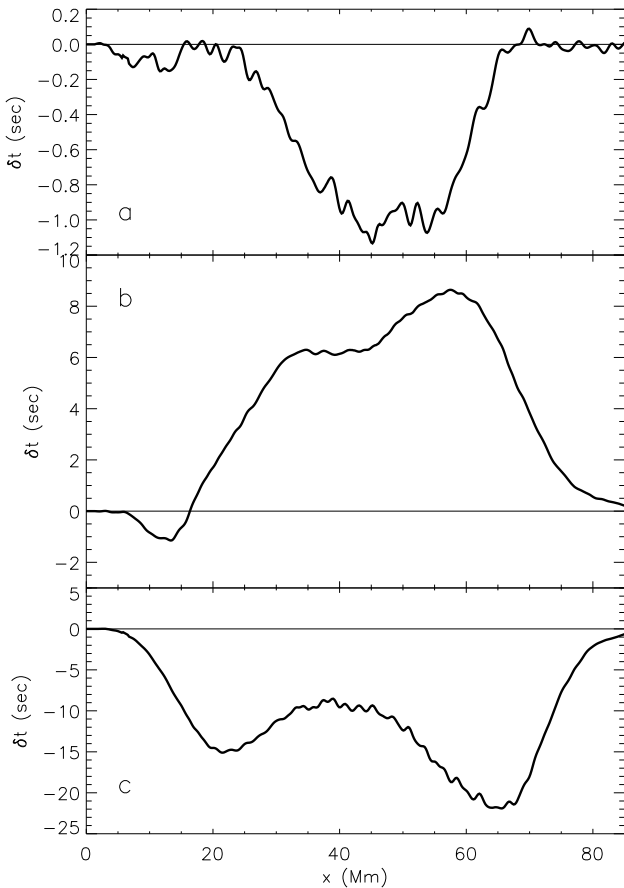


Fig. 18. Travel time difference plots computed for the first bounce for weak (case A), weakly curved strong (case B) and strongly curved strong (case C) magnetic field cases.

order bounces: these are approximately co-located with the loci of the lower turning points for the second and higher-order bounces, illustrated in Figs. 11, 13, 16.

Viewed as the focusing points for the generated waves, the caustics can be characterised by an increase of the power in the oscillations (Kravtsov & Orlov, 1993). Thus, the ratio of the power between the two cases can be expected to be most pronounced at such surfaces. This power increase is clearly observed in the time series (movies) of the simulated wave field, available in online material at <http://robertus.staff.shef.ac.uk/publications/acoustic/>. The magneto-acoustic mode generation and propagation is also clearly visible in the movies.

6. Conclusions

In this paper we presented the numerical modelling and helioseismological analysis of three physically different, localised magnetic field concentrations, mimicking sunspots in the solar photosphere. The model photosphere is based on the solar Standard Model S. The acoustic response of this quiet (non-magnetic) Sun model is close to that of the real Sun. The implemented magnetic fields for the simulations are different not only by their strength, but also by

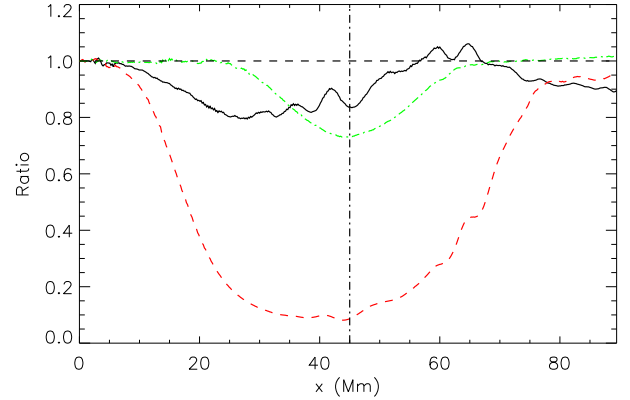


Fig. 19. Acoustic power absorption by the simulated sunspots. The green dash-dotted, black solid and red dashed curves correspond to the case A, case B and case C magnetic field configurations, respectively. Horizontal dashed line represents the power ratio 1. Vertical dash-dotted line shows the axis of the magnetic configuration.

the curvature of the field lines. The curvature of magnetic field creates magnetic tension, which consequently changes the pressure, density and temperature stratification of the equilibrium model. Three representative cases of magnetic fields in equilibrium with the external non-magnetic photospheric plasma are considered: weak magnetic field, strong but weakly-curved magnetic field and strongly-curved but strong magnetic field models. As a result of different magnetic field geometry, different temperature structures were obtained. In the case of weak magnetic field (Case A), the temperature deviation from the background is small, however, there is a complex structure of temperature decrease in the photosphere and temperature increase in the sub-photosphere. The two strong magnetic field cases (B and C) have the same magnetic field strength at the surface (3.5 kG). The case of the weakly-curved field (Case B) is characterised by the temperature decrease below the solar surface. However, the strongly-curved magnetic field (Case C) makes the temperature increased there.

The spatial structure of the models we used to carry out the simulations is such that it allows direct and easy comparison of the behaviour of the waves going through the non-magnetic plasma with the behaviour of the waves interacting with the magnetic field region. For that, we imposed magnetic field only in one half of the numerical domain, leaving the other half unaffected by magnetic field.

We analysed the three magnetic field cases by the means of local time-distance helioseismology. Synthetic time-distance, time-distance difference and travel time difference dependencies were calculated from the simulations. The dependencies show that the main part of effect of magnetic field on the acoustic wave is due to the change of the temperature structure in the sunspot. However, we also show that there is an energy leakage downwards in the model due to the wave mode conversion from purely acoustic to slow magneto-acoustic wave motion.

Despite the fact that the results are intrinsically correct up to the order of numerical noise amplitude, we acknowledge the disadvantage of their somewhat limited applicability. The simulations are carried out for a magnetic field and

background model, which are essentially two-dimensional. Thus, the main applicability limitation of our results consists in the energy distribution in the acoustic modes which is quantitatively (but not qualitatively, if only acoustic and magneto-acoustic waves are considered) different from the three-dimensional case. Also, the absorption of acoustic waves by a magnetic region in reality may be different from the one presented due to the difference in the acoustic energy distribution. However, since the sound and Alfvén speeds, and the other main magnetohydrodynamic parameters are not affected in any way by the dimensionality of the problem, the travel times and travel time differences are also independent on the dimensionality.

The two-dimensional magnetic fields used in the simulations presented in this paper can be extended to the three-dimensional cylindrically symmetric fields. However, simulations of acoustic wave propagation through three-dimensional magnetic structures requires significantly larger computing resources, so we leave such analysis for the nearest future.

7. Acknowledgments

This work was supported by a grant from the UK Science and Technology Facilities Council (STFC). RE acknowledges M. Kéray for patient encouragement. RE is also grateful to NSF, Hungary (OTKA, Ref.No. K67746). S. Zharkov acknowledges the support of the HELAS European Network.

References

- Crouch, A. D., & Cally, P. S. 2003, *Sol. Phys.*, 214, 201
 Cameron, R., Gizon, L., & Duvall, T. L., Jr. 2008, *Sol. Phys.*, 51
 Christensen-Dalsgaard, J., et al. 1996, *Science*, 272, 1286
 Duvall, T. L., Jr., et al. 1997, *Sol. Phys.*, 170, 63
 Gizon, L., & Birch, A. C. 2002, *ApJ*, 571, 966
 Gordovsky, M., & Jain, R. 2007, *ApJ*, 661, 586
 Hanasoge, S. M., Duvall, T. L., Jr., & Couvidat, S. 2007, *ApJ*, 664, 1234
 Hill, F., Lendenkov, O., Ehgamberdiev, S., & Chou, D.-Y. 2001, *SOHO 10/GONG 2000 Workshop: Helio- and Asteroseismology at the Dawn of the Millennium*, 464, 219
 Hughes, S. J., Rajaguru, S. P., & Thompson, M. J. 2005, *ApJ*, 627, 1040
 Kosovichev, A. G., & Duvall, T. L., Jr. 1997, *SCORE'96 : Solar Convection and Oscillations and their Relationship*, 225, 241
 Kravtsov, Y. A., & Orlov, Y. I. 1993, *Caustics, Catastrophes and Wave Fields by Yu. A. Kravtsov, Yu. I. Orlov* Berlin, GR: Springer-Verlag, 1993,
 Moradi, H., & Cally, P. S. 2008, *Sol. Phys.*, 251, 309
 Moradi, H., Hanasoge, S. M., & Cally, P. S. 2009, *ApJ*, 690, L72
 Nagashima, K., et al. 2007, *PASJ*, 59, 631
 Parchevsky, K. V., & Kosovichev, A. G. 2007, *ApJ*, 666, 547
 Schlüter, A., & Temesváry, S. 1958, *Electromagnetic Phenomena in Cosmical Physics*, 6, 263
 Schüssler, M., & Rempel, M. 2005, *A&A*, 441, 337
 Shelyag, S., Erdélyi, R., & Thompson, M. J. 2006, *ApJ*, 651, 576
 Shelyag, S., Erdélyi, R., & Thompson, M. J. 2007, *A&A*, 469, 1101
 Shelyag, S., Fedun, V., & Erdélyi, R. 2008, *A&A*, 486, 655
 Thompson, M. J., & Zharkov, S. 2008, *Sol. Phys.*, 251, 225
 Tóth, G., Keppens, R., & Botchev, M. A. 1998, *A&A*, 332, 1159
 Zharkov, S., Nicholas, C. J., & Thompson, M. J. 2007, *Astronomische Nachrichten*, 328, 240